Rapid Synthesis of Core/Shell ZnS:Mn/Si Nanotetrapods by a Catalyst-Free Thermal Evaporation Route

Soumitra Kar[†,*] **and Subhajit Biswas**

Department of Materials Science, Indian Association for the Cultivation of Science, Kolkata-700 032, India

ABSTRACT We report the fabrication of a hybrid all semiconductor core/shell nanotetrapod structure consisting of crystalline ZnS:Mn core and amorphous Si shell for the first time. The nanostructures were produced via a catalyst-free rapid thermal evaporation technique. Core/shell nanotetrapods were formed in two steps: (i) formation of the crystalline ZnS:Mn tetrapods and (ii) simultaneous surface adsorption of the in situ formed Si vapor species providing the amorphous shell. Crystalline tetrapod formation was guided by the formation of cubic structured ZnS octahedrons with four active (111) polar growth planes, which served as the favored growth site for the four wurtzite structured legs of the tetrapods. Choice of chloride salt as the source of dopant ion was crucial for the in situ generation of Si vapor. At elevated temperature, chloride salt reacted with the sulfur vapor to produce S_2Cl_2 gas that etched the Si wafers, generating Si vapor. Suppression of the surface-state-related blue emission was observed in the core/shell structures that clearly supported the formation of a shell layer. Elimination of the surface states ensured efficient energy transfer to the dopant Mn ionic state, resulting in the strong orange emission via $^4T_1-^6A_1$ electronic transition.

KEYWORDS: core/shell nanostructures • tetrapods • zinc sulfide • photoluminescence

INTRODUCTION

The ability to systematically manipulate the inorganic nanocrystals remains an important goal in modern materials chemistry. Shapes and sizes of the inorganic nanocrystals control their widely varying electrical and optical properties (1−13). Tetrapod-shaped nanocrystals present promising potential as building blocks for solar cells (14, 15), active components in nanoscale transistors (16), etc. Tetrapod structures of different inorganic materials such as ZnO, CdS, CdSe, and CdTe (17−21) have been widely studied in recent times to explore different physical and structural properties. However, there are only a few report on ZnS tetrapods (22−24). The lack of extensive study on ZnS tetrapods could be attributed to difficulties associated with the synthesis of such kind of nanostructures. Because surface defects in nanostructures are prominently due to large surface to volume ratio, the efficiency of nanostructures and hence their performance in nanodevices could be improved by reducing surface defects (25−30). Thus the current focus is on developing synthesis strategies for effective surface passivation of 1D nanostructure that minimizes surface defects by creation of core/shell heterostructures.

Zinc sulfide, a typical II−VI compound semiconductor, is an important optoelectronic device material because of its wide direct band gap of 3.77 eV (2, 31−34). It is well-known that ZnS doped with manganese (Mn) exhibits attractive light-emitting properties with increased optically active sites for applications as efficient phosphors (35, 36). Interesting fluorescence, magnetic, and magneto-optical properties of the Mn^{2+} ions incorporated ZnS nanostructures (31, 37−43) demands more research on controlled fabrication of technologically important nanostructures such as ZnS:Mn tetrapods. Again, fabricating a suitable shell layer is important to prevent the oxidation of the nanostructures or to avoid interference in the building blocks of a complex nanosclae circuit. There are a few reports on putting a amorphous silica (SiO_2) shell on the semiconductor nanostructures (44−46). For the application purpose, it is more advantageous to have a semiconducting shell compared to dielectric materials silica. There are a few reports on the biaxial ZnS-Si nanowires, where crystalline ZnS and Si layers grew side-by-side (47, 48). However, these structures are not capable of fully eliminating the surface defects. Recently we have reported (49) a crystalline Ag core/amorphous Si shell heterostructured nanowires. Thus fabricating an all semiconductor core/shell tetrapod structure is still a challenge.

In this article, we report a catalyst-free rapid thermal evaporation route to synthesize ZnS:Mn/Si core/shell nanotetrapods. The nanostructures consisted of a single-crystalline ZnS:Mn core surrounded by an amorphous Si shell. Growth mechanism of the dopant based core/shell nanotetrapods have been studied and discussed here. The photoluminescence property of the core/shell nanotetrapods were studied in detail. To the best of our knowledge, this is the first report on the fabrication of dopant-based core/shell ZnS nanotetrapods.

---

* Author to whom any correspondence should be addressed. Tel.: (407) 882-2848. Fax: (407) 882-2819. E-mail: kar_mitra@yahoo.co.in.

Received for review February 26, 2009 and accepted May 27, 2009

[†] Present Address: NanoScience Technology Center, University of Central Florida, Orlando, Florida 32826.

DOI: 10.1021/am900123x

EXPERIMENTAL PROCEDURE

For the synthesis of the undoped and doped ZnS nanostructures, analytical grade Zn, S, and $MnCl_2$ powders were used as the precursors. A conventional horizontal quartz tube furnace fitted with a gas flow system at one end and a rotary vacuum pump at the other end was used for the synthesis. Ultrasonically cleaned Si wafers (1/1 cm) were used as the substrate for deposition of the nanostructures. The three precursors and the substrate were placed in four separate places inside the quartz tube. Starting with the upstream end S, $MnCl_2$, Zn, and Si substrate were placed at different temperature zones maintaining a fixed distances in between. Zn powder was placed at the central zone at 750 °C and the Si substrate was placed at the same temperature but 2 cm away toward the downstream end. S powder was placed at 400 °C 20 cm from the Zn powder at the upstream end. $MnCl_2$ was placed in between S and Zn powder. Four different atomic ratios of the Mn to Zn precursors (Mn:Zn = 0:1, 1:4, 3:8, 1:2) were employed. In the subsequent discussion, the resulting samples are referred as S-1, S-2, S-3, and S-4 for the precursor ratios Mn:Zn = 0:1, 1:4, 3:8, and 1:2, respectively. After evacuating the quartz tube up to $\sim 1 \times 10^{-3}$ Torr, we passed Ar gas through it with a flow rate of 100 cm^3/min for the entire deposition period. After 15 min of deposition, the quartz tube was taken out of the furnace to allow rapid cooling to room temperature. Thick white depositions were found on the substrates and characterized with different techniques. Syntheses were also carried out for 5 min to investigate the growth mechanism.

The products were characterized using Seifert 3000P X-ray diffractometer with Cu Kα radiation. Microstructures of the nanoforms were obtained by scanning electron microscopy (Hitachi S-2300) and transmission electron microscopy (TEM, JEM 2010). Crystal structure of the products was also studied through the high-resolution transmission electron microscopy (HRTEM, JEM 2010). Photoluminescence (PL) measurements were carried out at room temperature with 325 nm excitation wavelengths using a (Hitachi F-2500) luminescence spectrometer. Electron paramagnetic resonance study of the powder sample was done with Varian E-109C X-band spectrometer.

RESULTS AND DISCUSSIONS

The morphologies of the white products deposited on the Si substrates were characterized through SEM. Figure 1a shows that tetrapod like nanostructures were formed in absence of Mn source. The crystallograpic angle between the legs should be 109.5°. The two-dimensional projection of the tetrapods in the SEM image recorded perpendicular to the fourth leg shows three legs in one plane with ~120° angle between the legs. The diameters of the legs of the ZnS nanotetrapods varied within 80−150 nm and lengths varied within 500 and 800 nm. The SEM images depicted in images b and c Figure 1 show that the introduction of the Mn source in the deposition chamber did not affect the morphology of the nanostructures. Images b and c in Figure 1 shows the morphology of S-2 and S-4 (i.e., the products synthesized with Mn:Zn = 1:4 and 1:2 atomic ratios, respectively). Although the morphology of the products and lengths of the individual legs remained unaltered, the diameters of the legs increased significantly after Mn doping. The higher-magnification image shown in the inset of Figure 1b exhibits the triangular cross-section of the tetrapod leg. The diameters of the legs of these tetrapods remained almost unaffected to the different amount of Mn incorporations. The sample synthesized for 5 min of deposition time shows the formation of particlelike features. These nanostructures were studied in detail by TEM and the results are discussed later.

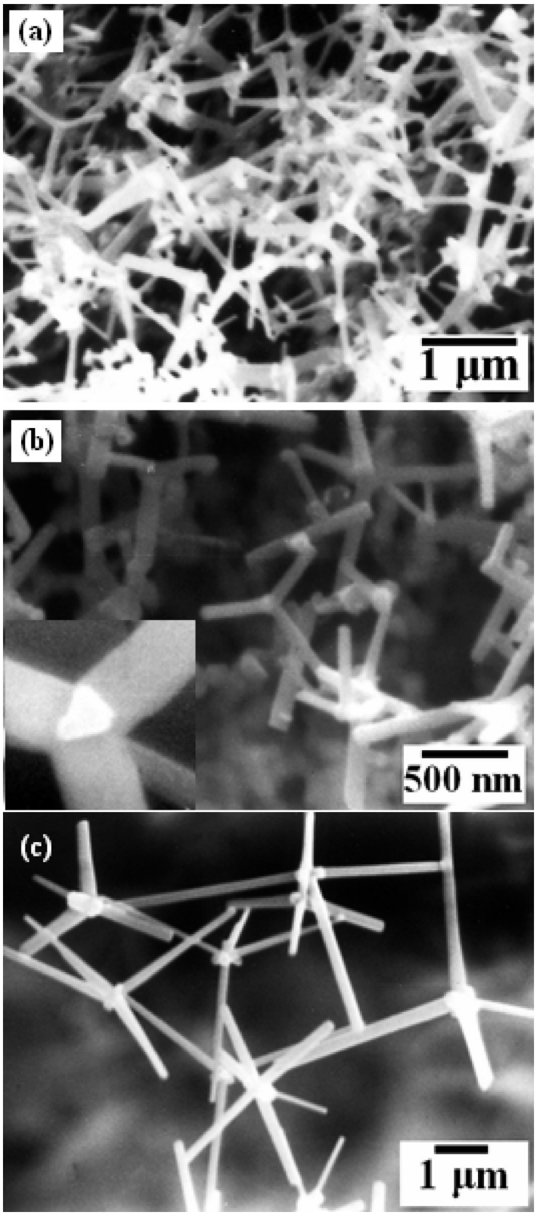

FIGURE 1. SEM images of the sample (a) S-1, (b) S-2, and (c) S-4 synthesized Mn:Zn = 0:1, 1:4, and 1:2 respectively.

The samples were characterized by XRD to reveal their crystalline phase. The XRD pattern of the pure ZnS tetrapod sample (S-1) exhibited pure hexagonal wurtzite phase, as all the XRD peaks were indexed to those of the hexagonal wurtzite ZnS. XRD patterns of the doped samples (S-2, S-3, and S-4) also showed the formation of wurtzite ZnS. No additional peaks corresponding to any other impurity phases such as MnS were detected in the doped samples. Figure 2i shows a representative XRD pattern recorded on the Mn-doped nanotetrapod samples synthesized with the highest amount of Mn source (S-4). All the XRD peaks were indexed to the hexagonal wurtzite ZnS with the lattice constants a = 3.816 Å and c = 6.253 Å, in good agreement with the standard values reported in JCPDS (Joint Committee on Powder Diffraction Standards, Card no. 36−1450). The

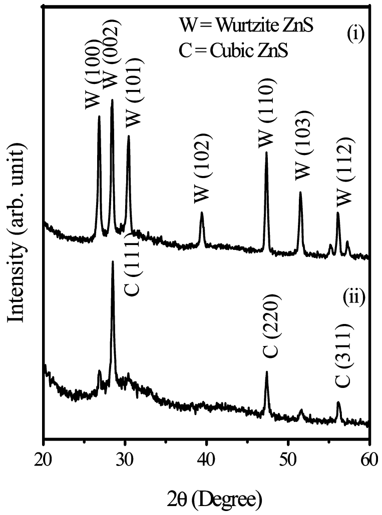

FIGURE 2. XRD patterns revealing the hexagonal wurtzite phase and cubic zinc blende phase of ZnS synthesized at 750 °C for (i) 15 and (ii) 5 min.

sharp XRD peaks imply good crystallinity of the products. No peak corresponding to MnS is detected in the XRD pattern. The XRD pattern of the sample synthesized with highest amounts of Mn source (Mn:Zn = 1:2) is selected here, with a view to show that phase-pure ZnS was formed up to this limit of Mn source. The XRD patterns of the samples synthesized with more Mn amounts (Mn:Zn > 1:2) revealed the formation of MnS phases along with the ZnS phases. Thus we have restricted our studies up to the Mn: Zn = 1:2 values. To investigate the growth mechanism of ZnS nanotetrapods, we also carried out experiments for 5 min with Mn:Zn= 0:1 and 1:2, respectively. Both the samples showed quite similar XRD patterns and Figure 2ii shows the pattern for the doped sample. Interestingly, the XRD peaks are predominantly indexed to the zinc blende phase of ZnS, as the intensity of the peak at ~28.43° (i.e., cubic (111) plane) is much stronger compared to the hexagonal phase related peaks at $2\theta \approx 26.92$ and 30.43°, respectively. Also, the absence of the peak corresponding to the (102) plane of wurtzite ZnS at $2\theta \approx 39.4°$ for this sample implies the formation of a cubic-phase-dominated sample. The plausible reason behind the difference between the crystalline phases of the nanostructures obtained after different deposition periods will be discussed later in the growth mechanism section.

Elementary compositions of the tetrapods were studied by EDAX. EDAX analysis of the undoped ZnS sample (S-1) reveals the presence of only Zn and S as the constituent elements in near stoichiometric ratio (Zn:S = 52.4:47.6). But EDAX spectra of the doped samples revealed (not shown here) the presence of significant amounts of Si along with the Zn, S, and Mn. The reasons behind the appearance of the Si peak in the EDAX spectra of the doped tetrapod samples was investigated through TEM and HRTEM studies and EDAX setup integrated with the TEM. Details are discussed later. From the elementary compositional analyses, the relative percentages of Mn to that of Zn were calculated. 1.5, 5, and 9 at % of Mn compared to that of Zn were detected in the samples synthesized with initial precursor ratio of Mn:Zn = 1:4 (S-2), 3:8 (S-3), and 1:2 (S-4), respectively.

The structure and morphology of the samples were further characterized by TEM. Figure 3a shows the TEM image of an undoped ZnS nanotetrapod. Four legs of the ZnS tetrapod were protruding from the center to form the tetrapod structure. The HRTEM image of a single leg of the tetrapod is shown in Figure 3b. The measured spacing of the lattice fringes was 0.330 nm, which corresponds to the (100) lattice plane of wurtzite ZnS. No crystal defects such as dislocation or stacking faults were observed along the leg in the high-resolution image. So the growth direction of the leg was along the crystallographic axis of ⟨001⟩. The fast Fourier transform (FFT) pattern in the inset also confirms the single-crystalline nature of the tetrapod leg and the growth direction along ⟨001⟩. The TEM image of a representative Mn doped ZnS (S-2, Mn:Zn = 1:4) nanotetrapod is shown in Figure 3c. Closer observation of the TEM image reveals the triangular cross-section of the leg of the tetrapod (shown separately in the inset of Figure 3c). The image clearly demonstrates the presence of an amorphous shell layer surrounding the crystalline core part. The HRTEM image of a single leg is depicted in Figure 3d, producing clear evidence of the core/shell nature of the doped nanotetrapods. The SAED pattern in the inset confirms the growth direction of the leg to be ⟨001⟩. The diffused ring in the SAED pattern represents the amorphous shell part of the tetrapods. The EDAX signal recorded separately on the amorphous shell confirmed its composition as Si. Several EDAX spectra recorded on different tetrapods did not show the presence of any appreciable amount of O. Thus the amorphous shell surrounding the Mn doped ZnS nanotetrapods could be assigned as amorphous Si.

TEM and HRTEM images shown in Figure 4 reveals the morphology and crystal structure of the nanoforms obtained at the early stage of the growth of the nanotetrapods. Figure 4a depicts the preliminary growth stage of the undoped and Mn-doped tetrapod structures, respectively. Formation of octahedral nucleus is obvious from the images. The magnified TEM image of one nanoparticle is shown in the inset of Figure 4a, confirming the octahedral shape of the particles. The HRTEM image of one of these octahedral nucleuses is presented in Figure 4b. The image reveals the cubic crystal structure of ZnS. The lattice spacing was measured as 3.12 Å, which represents the (111) plane of cubic ZnS. The FFT pattern shown in the inset also indicated the formation of cubic ZnS. TEM investigations on the 5 min deposited Mn-doped ZnS samples also showed the formation of similar octahedral shaped nucleus. But, the doped nucleuses were covered by an amorphous shell. Figure 4c shows one representative Mn doped ZnS (Mn:Zn in 1:4 atomic ratio) sample at their early stage of growth. HRTEM image of one such nucleus is shown in Figure 4d. Presence of the amorphous shell is clearly visible in this image. Both the wurtzite and cubic polytype of ZnS are observed in this image.

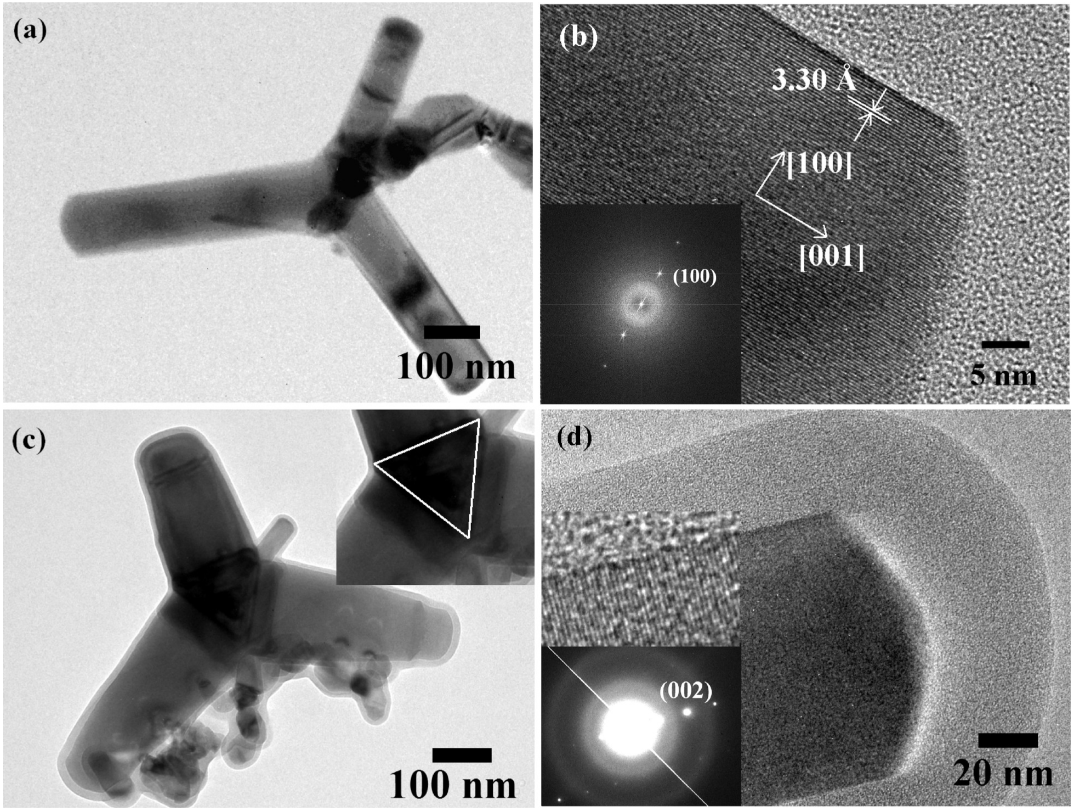

FIGURE 3. (a) TEM image of a single undoped ZnS tetrapod. (b) HRTEM image of one leg of the ZnS tetrapod along with the FFT pattern in the inset. (c) TEM image of a single Mn-doped core/shell nanotetrapod. Magnified image in the inset shows the triangular cross-section of the leg. (d) HRTEM image of the leg of the ZnS:Mn/Si tetrapod showing crystalline ZnS:Mn core surrounded by an amorphous Si shell. Inset shows the SAED pattern and a selected magnified portion of the crystalline core.

Appearance of the wurtzite zone could be ascribed to the early stage of the formation the wurtzite legs.

The growth mechanism of the core/shell tetrapods could be explained in two steps: (i) nucleation and growth of tetrapods and (ii) formation of amorphous Si shell surrounding the crystalline ZnS:Mn core. The wurtzite polytype of ZnS is stable above (1035 °C) (34) whereas cubic crystal structure is stable at lower temperature. Because the temperature of the deposition zone (750 °C) is well below the phase transition temperature between the hexagonal and cubic structure of ZnS, the products initially nucleates in cubic phase. We believe that the cubic structured octahedron nucleus was the growth unit of the teatrapod structure. The growth mechanism of the ZnS tetrapod structures is depicted schematically in Figure 5a. The XRD and HRTEM studies already revealed the formation of cubic crystal. Thus, we propose that during the rapid condensation of the ZnS vapor species, octahedron nuclei with cubic crystal structure were formed. In ZnS, Zn and S atoms were arranged with one Zn atom tetrahedrally coordinated to four S atoms. Thus the ⟨111⟩ direction of the cubic ZnS and ⟨001⟩ direction of wurtzite ZnS are crystallographically polar. Thus the eight triangular facets of the tetrahedron were along the ⟨111⟩ direction and out of the eight planes four are Zn terminated and remaining four are S-terminated. As the Zn-terminated surfaces are more active than the sulfur terminated one, the growth will continue along the four directions, introducing the tetrapod structure. After a critical size limit, this growth along the ⟨111⟩ direction of the cubic structure becomes unstable, and a stable wurtzite crystal structure growth will prevail along the ⟨001⟩ direction (22). The crystallographic changes might follow by several structural defects such as staking faults. These changes in crystallographic orientation resulted in the formation of the tetrapod structure with four hexagonal wurtzite legs. Because the well-defined facets were the lowest-energy surfaces, formation of facets were often observed during the rapid crystal growth.

To understand the amorphous shell formation mechanism, it should be noted that the shelling process was doping-dependent. This clearly indicated that the chloride precursor $MnCl_2$ played a critical role in the formation of the amorphous shell layer. $MnCl_2$ reacted with the S vapor to produce MnS as well as a toxic gas S_2Cl_2 following eq 1. A portion of the MnS vapor got diffused through the ZnS crystals to provide Mn doping. The gaseous byproduct S_2Cl_2 is a toxic material and also acts as an erosion reagent of Si (49). To eliminate the risk of toxic exposure, the gas outlet of the reaction chamber was passed through NaOH solution. The toxic S_2Cl_2 gas reacted with NaOH to produce non toxic compounds following reaction 2.

$$MnCl_2 + 3S = MnS + S_2Cl_2 \qquad (1)$$

$$2S_2Cl_2 + 6NaOH = 4NaCl + 3S + Na_2SO_3 + 3H_2O \quad (2)$$

The exposed surface of the Si wafer was partially etched by the toxic S_2Cl_2 gas producing elementary Si vapor species. The surface regions surrounding the growth front of the tetrapods were at higher energy states because of structural reconstruction. The higher-energy growth front of the tetrapod structure served as the favored sites for the adsorption of the atomic Si species. A relatively low synthesis temperature (750 °C) might have prevented ZnS−Si alloy formation. Zhan et al. (47) have also reported phase-separated growth of a side-by-side layer of crystalline ZnS and crystalline Si composite nanowires at 1100 °C. Because of higher mobility at high temperature, these Si species migrate, surrounding the surface and providing a uniform surface layers. Formation of the amorphous Si shell is depicted schematically in Figure 5b. With a continuous supply of the constituent elements, the ZnS:Mn tetrapod legs grew in length followed by Si shell layer deposition. As the reaction stopped, a decrease in temperature resulted in the discontinuation of the supply of the constituent elements restricting further growth of the core ZnS:Mn part. However, the already-formed S_2Cl_2 gas generated enough Si vapors that fully coated the core part. When the reaction was prematurely stopped, the tetrapod legs could not be formed because of the lack of constituent elements. On the other hand, the already-formed Si species get deposited on the higher-energy surfaces and migrate throughout the surface to completely over coat the resultant nanostructures.

Photoluminescence measurements were carried out at room temperature with 325 nm as the excitation wavelength (Figure 6). A strong broad blue emission peak centered at ~465 nm was observed for all the samples synthesized with or without $MnCl_2$. This blue emission band could be attributed to the trapped luminescence arising from the surface states of ZnS (50). The Mn-doped tetrapod samples also exhibited characteristic orange emission band at around 590 nm. The origin of this orange emission is attributed to the $^4T_1-^6A_1$ transition of the Mn^{2+} (37, 38, 41, 50, 51). The increase in the intensity of the peak with Mn^{2+} concentration is due to the formation of more and more Mn^{2+} luminescent centers, whereas the quenching of the orange luminescence at highest Mn concentration was due to the interaction of the neighboring Mn^{2+} ions at the nearest, the second nearest, and probably at the third nearest neighbor sites (37, 38). The intensity of the blue emission is quenched appreciably when the nanotetrapods are doped with Mn^{2+}. This could be attributed to the formation of amorphous Si shell which is expected to eliminate the surface states. In addition, elimination of the surface states ensured efficient energy transfer to the 3d states ($^4T_1$) of Mn ions. Considerable increase of doping percentage led to an increase in the Mn^{2+} centers and as a result an increase in the intensity of the orange emission.

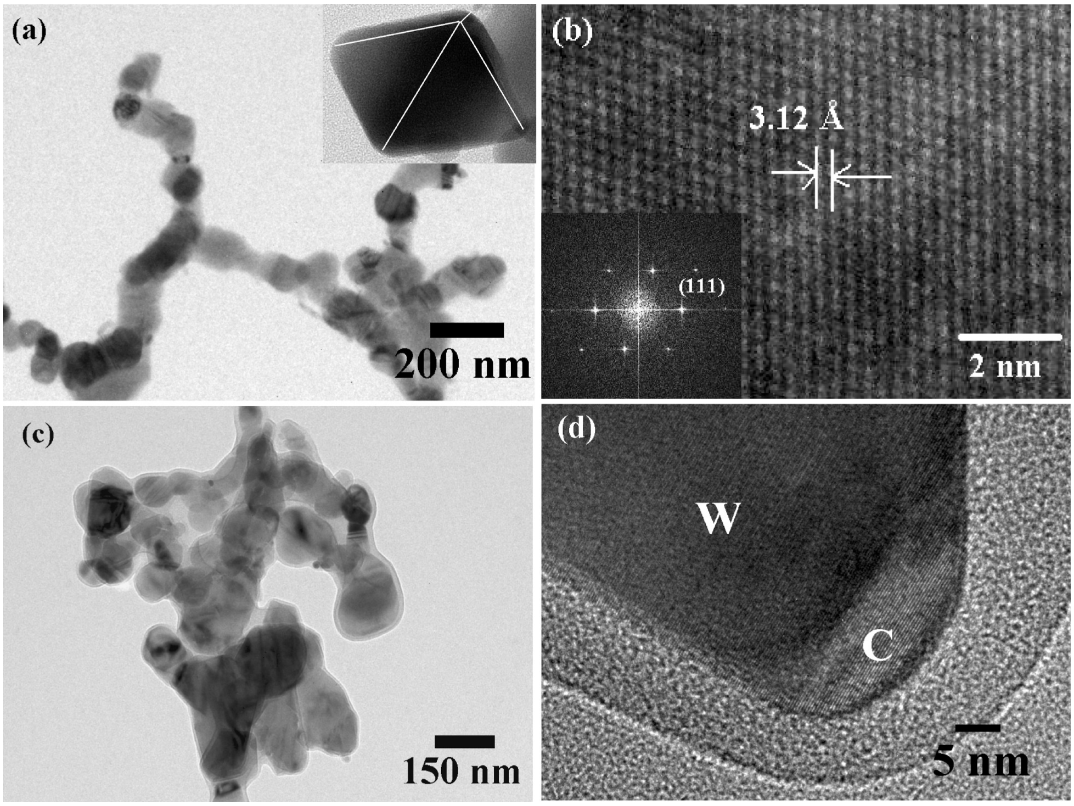

FIGURE 4. TEM images of the tetrahedral nucleus formed after 5 min deposition: (a, b) undoped ZnS and (c, d) ZnS:Mn sample. Image in part (b) shows the cubic structure of the ZnS tetrahedron with the corresponding FFT pattern in the inset, whereas (d) shows the HRTEM image ZnS:Mn nucleus. Wurtzite (W) and cubic (C) crystalline zone are identified in this image. Inset shows the SAED pattern and a selected magnified portion of the crystalline core.

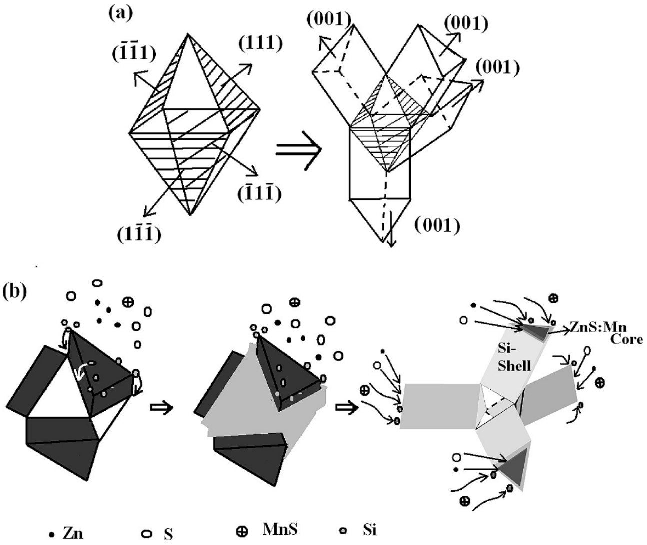

FIGURE 5. Schematic diagram of the growth of the (a) ZnS tetrapod structure and (b) ZnS:Mn/Si core/shell tetrapods.

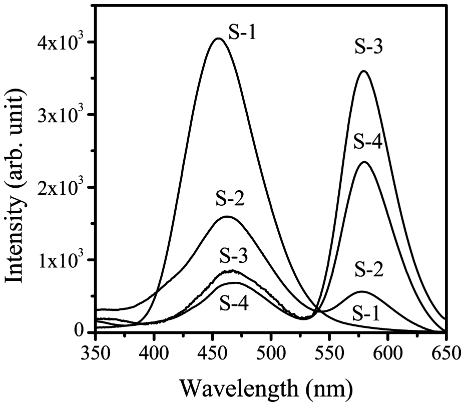

FIGURE 6. Photoluminescence spectra of the ZnS and ZnS:Mn/Si nanotetrapods.

The proper doping of the manganese ions inside the ZnS core of the doped tetrapod samples could be proved beyond doubt by analyzing the EPR spectra. Manganese introduced in to the ZnS host lattice is expected to generate different sinal from those deposited outside the ZnS crystals because the hyperfine splitting constants depend on the environment of Mn ions, the bonding characteristics between Mn ions and host lattice can be explained by EPR analysis. The Mn^{2+} charge state has a half filled d shell (3d (5)) with angular momentum $L = 0$ and spin $S = 5/2$. The distinctive feature of EPR of Mn is its hyperfine splitting arising from ^{55}Mn nucleus ($I = 5/2$). Here, the spin Hamiltonian can be written as

$$H = g\beta \mathbf{H}\cdot\mathbf{S} + |A|\mathbf{S}\cdot\mathbf{I} + 1/6a(S_x^4 + S_y^4 + S_z^4) + D[S_z^2 - 1/3S(S + 1)]$$

Here, β is the Bohr magneton, H is the applied magnetic field, and g, D, and $|A|$ are the EPR parameters. The first term in the equation is due to Zeeman interaction, the second to hyperfine interaction with the Mn nucleus, the third to cubic field, and the fourth to fine structure splitting.

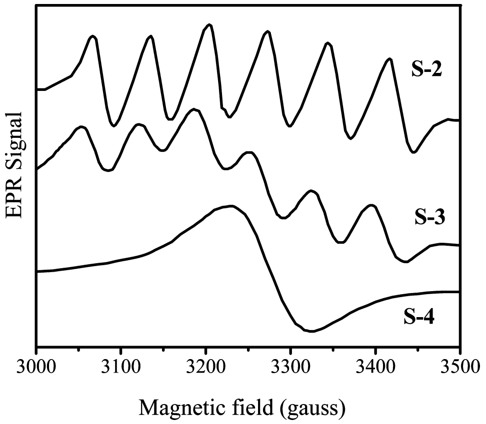

FIGURE 7. EPR spectra of the ZnS:Mn/Si core/shell nanotetrapods.

Figure 7 shows the EPR spectra of the representative Mn-doped ZnS tetrapods. Typical six-line hyperfine structures appeared for the 1.5 at % Mn-doped ZnS tetrapods (S-2). At very low Mn concentration, this spectral feature arose because of |−1/2> to |1/2> transition coupled to Mn nuclear spin ($I = 5/2$), as few Mn^{2+} ions isolated from each other were distributed inside the ZnS nanorod lattice. But for S-3 with actual Mn/Zn = 0.05, the EPR spectrum appeared with two kinds of Mn^{2+} centers. One component of the spectra was due to Mn^{2+} ions and had six hyperfine lines, whereas the other was due to the formation of small Mn clusters, resulting in a broad resonance line. At higher Mn concentrations, the density of Mn^{2+} ions introduced within the ZnS nanorod lattice increased to such value that they started interacting with each other and the resulting Mn−Mn interaction started influencing the EPR results. The sample S-4 with estimated Mn/Zn = 0.09, i.e., the more Mn-incorporated tetrapod sample exhibited a single Lorentzian-shaped spectrum. This broad line can be attributed to clustered manganese ions, which strongly influence one another through their magnetic moments. The sharp drop in photoluminescence intensity for higher percentage of Mn-doped sample (Figure 6) could be explained with the help of EPR results. The extensive broadening of the EPR spectrum could be attributed to the enhanced Mn−Mn coupling.

Thus the present study demonstrates a simple strategy to synthesize high-quality core/shell tetrapod structure. This synthesis strategy could be extended to synthesize other potentially important all-semiconductor core/shell nanostructures. This all-semiconductor core/shell approach compare to the existing semiconductor core and dielectric or ceramic oxide shell could be beneficial in fabricating device structures. The formation of effective shell layer over the Mn doped ZnS tetrapod core could provide efficient bright nanomaterials for display devices.

CONCLUSION

In summary, ZnS nanotetrapods and ZnS:Mn/Si core/shell nanotetrapods were synthesized by a rapid thermal evaporation technique. The chlorides precursor of the dopant ions produced a toxic gaseous by product S_2Cl_2 upon reaction with S. This toxic gas etched the Si substrate to produce Si vapor that gets adsorbed on the growth sites of the ZnS:Mn tetrapods, producing the amorphous shell. The Mn-doped core/shell nanotetrapods exhibited yellow/orange emission at the room temperature.

Acknowledgment. Authors like to dedicate this paper to the memory of late Prof. Subhadra Chaudhuri, Department of Materials Science, Indian Association for the Cultivation of Science India.

REFERENCES AND NOTES

(1) Alivisatos, A. P. *Science* **1996**, *271*, 933.
(2) Kar, S.; Chaudhuri, S. *J. Phys. Chem. B* **2005**, *109*, 3298.
(3) Kar, S.; Chaudhuri, S. *Synth. React. Inorg., Met.-Org., Nano-Met. Chem.* **2006**, *36*, 289.
(4) Kar, S.; Pal, B. N.; Chaudhuri, S.; Chakravorty, D. *J. Phys. Chem. B* **2006**, *110*, 4605.
(5) Lieber, C. M. *Solid State Commun.* **1998**, *107*, 607.
(6) Kamat, P. V. *J. Phys. Chem. C* **2008**, *112*, 18737.
(7) Rao, C. N. R.; Vivekchand, S. R. C.; Biswasa, K.; Govindaraja, A. *Dalton Trans.* **2007**, 3728.
(8) Kamat, P. V. *J. Phys. Chem. C* **2007**, *111*, 2834.
(9) Xia, Y. N.; Yang, P. D.; Sun, Y. G.; Wu, Y. Y.; Mayers, B.; Gates, B.; Yin, Y. D.; Kim, F.; Yan, Y. Q. *Adv. Mater.* **2003**, *15*, 353.
(10) Rao, C. N. R.; Deepak, F. L.; Gundiah, G.; Govindaraj, A. *Prog. Solid State Chem.* **2003**, *31*, 5.
(11) Biswas, S.; Kar, S. *Nanotechnology* **2008**, *19*, 045710.
(12) Kar, S.; Dev, A.; Chaudhuri, S. *J. Phys. Chem. B* **2006**, *110*, 17848.
(13) Kar, S.; Chaudhuri, S. *J. Phys. Chem. B* **2006**, *110*, 4542.
(14) Huynh, W. U.; Dittmer, J. J.; Alivisatos, A. P. *Science* **2002**, *295*, 2425.
(15) Sun, B. Q.; Marx, E.; Greenham, N. C. *Nano Lett.* **2003**, *3*, 961.
(16) Li, J. B.; Wang, L. W. *Nano Lett.* **2003**, *3*, 101.
(17) Ghoshal, T.; Kar, S.; Biswas, S.; Majumdar, G.; Chaudhuri, S. *J. Nanosci. Nanotechnol.* **2007**, *7*, 689.
(18) Dai, Y.; Zhang, Y.; Li, Q. K.; Nan, C. W. *Chem. Phys. Lett.* **2002**, *358*, 83.
(19) Jun, Y. W.; Lee, S. M.; Kang, N. J.; Cheon, J. *J. Am. Chem. Soc.* **2001**, *123*, 5150.
(20) Manna, L.; Milliron, D. J.; Meisel, A.; Scher, E. C.; Alivisatos, A. P. *Nat. Mater.* **2003**, *2*, 382.
(21) Manna, L.; Scher, E. C.; Alivisatos, A. P. *J. Am. Chem. Soc.* **2000**, *122*, 12700.
(22) Kar, S.; Santra, S.; Chaudhuri, S. *J. Nanosci. Nanotechnol.* **2008**, *8*, 3222.
(23) Oneil, M.; Marohn, J.; McLendon, G. *J. Phys. Chem.* **1990**, *94*, 4356.
(24) Zhu, Y. C.; Bando, Y.; Xue, D. F.; Golberg, D. *J. Am. Chem. Soc.* **2003**, *125*, 16196.
(25) Lauhon, L. J.; Gudiksen, M. S.; Wang, C. L.; Lieber, C. M. *Nature* **2002**, *420*, 57.
(26) Nirmal, M.; Brus, L. *Acc. Chem. Res.* **1999**, *32*, 407.
(27) Bruchez, M.; Moronne, M.; Gin, P.; Weiss, S.; Alivisatos, A. P. *Science* **1998**, *281*, 2013.
(28) Chan, W. C. W.; Nie, S. M. *Science* **1998**, *281*, 2016.
(29) Klimov, V. I.; Mikhailovsky, A. A.; Xu, S.; Malko, A.; Hollingsworth, J. A.; Leatherdale, C. A.; Eisler, H. J.; Bawendi, M. G. *Science* **2000**, *290*, 314.
(30) Kar, S.; Santra, S.; Heinrich, H. *J. Phys. Chem. C* **2008**, *112*, 4036.
(31) Kar, S.; Biswas, S. *J. Phys. Chem. C* **2008**, *112*, 11144.
(32) Kar, S.; Biswas, S.; Chaudhuri, S. *Nanotechnology* **2005**, *16*, 737.
(33) Ong, H. C.; Chang, R. P. H. *Appl. Phys. Lett.* **2001**, *79*, 3612.
(34) Kar, S.; Chaudhuri, S. *Chem. Phys. Lett.* **2005**, *414*, 40.
(35) Chen, W.; Sammynaiken, R.; Huang, Y. N.; Malm, J. O.; Wallenberg, R.; Bovin, J. O.; Zwiller, V.; Kotov, N. A. *J. Appl. Phys.* **2001**, *89*, 1120.
(36) Dinsmore, A. D.; Hsu, D. S.; Qadri, S. B.; Cross, J. O.; Kennedy, T. A.; Gray, H. F.; Ratna, B. R. *J. Appl. Phys.* **2000**, *88*, 4985.
(37) Bhargava, R. N.; Gallagher, D.; Hong, X.; Nurmikko, A. *Phys. Rev. Lett.* **1994**, *72*, 416.
(38) Biswas, S.; Kar, S.; Chaudhuri, S. *J. Phys. Chem. B* **2005**, *109*, 17526.
(39) Biswas, S.; Kar, S.; Chaudhuri, S.; Nambissan, P. M. G. *J. Phys.: Condens. Matter* **2008**, *20*, 235226.
(40) Kar, S.; Biswas, S.; Chaudhuri, S. *Synth. React. Inorg., Met.-Org., Nano-Met. Chem.* **2006**, *36*, 193.
(41) Kar, S.; Biswas, S.; Chaudhuri, S.; Nambissan, P. M. G. *Nanotechnology* **2007**, *18*, 225606.
(42) Biswas, S.; Ghoshal, T.; Kar, S.; Chakrabarti, S.; Chaudhuri, S. *Cryst. Growth Des.* **2008**, *8*, 2171.
(43) Sapra, S.; Prakash, A.; Ghangrekar, A.; Periasamy, N.; Sarma, D. D. *J. Phys. Chem. B* **2005**, *109*, 1663.
(44) Li, Y.; Ye, C. H.; Fang, X. S.; Yang, L.; Xiao, Y. H.; Zhang, L. D. *Nanotechnology* **2005**, *16*, 501.
(45) Shen, G. Z.; Bando, Y.; Tang, C. C.; Golberg, D. *J. Phys. Chem. B* **2006**, *110*, 7199.
(46) Moore, D.; Morber, J. R.; Snyder, R. L.; Wang, Z. L. *J. Phys. Chem. C* **2008**, *112*, 2895.
(47) Zhan, J. H.; Bando, Y.; Hu, J. Q.; Sekiguchi, T.; Golberg, D. *Adv. Mater.* **2005**, *17*, 225.
(48) Hu, J. Q.; Bando, Y.; Liu, Z. W.; Sekiguchi, T.; Golberg, D.; Zhan, J. H. *J. Am. Chem. Soc.* **2003**, *125*, 11306.
(49) Ghoshal, T.; Biswas, S.; Kar, S. *J. Phys. Chem. C* **2008**, *112*, 20138.
(50) Bol, A. A.; Meijerink, A. *Phys. Rev. B* **1998**, *58*, R15997.
(51) Sarkar, I.; Sanyal, M. K.; Kar, S.; Biswas, S.; Banerjee, S.; Chaudhuri, S.; Takeyama, S.; Mino, H.; Komori, F. *Phys. Rev. B* **2007**, *75*, 224409.

AM900123X